Tan, Hongwei; Bhattacharya, Sayani; Qin, QiHang; Lahtinen, Jouko; van Dijken, Sebastiaan

Mimicking Neurotransmitter Release and Long-Term Plasticity by Oxygen Vacancy Migration in a Tunnel Junction Memristor

Published in:
Advanced Intelligent Systems

DOI:
10.1002/aisy.201900036

Published: 24/06/2019

Document Version
Publisher's PDF, also known as Version of record

ADVANCED INTELLIGENT SYSTEMS
Open Access
www.advintellsyst.com

Mimicking Neurotransmitter Release and Long-Term Plasticity by Oxygen Vacancy Migration in a Tunnel Junction Memristor

Hongwei Tan, Sayani Majumdar, Qihang Qin, Jouko Lahtinen, and Sebastiaan van Dijken**

Activated by action potentials and Ca^{2+} ion migration, neurotransmitters in biological synapses are released from vesicles at the presynaptic membrane to the cleft and bonded to receptors on the postsynaptic membrane. The bonded neurotransmitters modify the electrochemical properties of the postsynaptic membrane and, thereby, the synaptic plasticity, which forms the basis for learning, memory, emotion, cognition, and consciousness. Here, the oxygen vacancy transport in Au/$SrTiO_3$ (STO)/$La_{0.67}Sr_{0.33}MnO_3$ (LSMO) tunnel junctions is exploited to mimic neurotransmission processes in an artificial ionic electronic device. Using voltage pulses of varying number, amplitude, and polarity, it is demonstrated that reversible oxygen vacancy migration across the STO/LSMO interface provides stable multilevel resistance switching for octal memory devices and resembles the quantal, stochastic, and excitatory or inhibitory nature of neurotransmitter release dynamics. Moreover, fundamental synaptic behaviors including long-term potentiation/depression and various types of spike-timing-dependent plasticity characteristics are emulated, opening a promising biorealistic approach to the design of neuromorphic devices.

1. Introduction

Adaptive synaptic plasticity is crucial for key brain functions, including learning, memory, and cognition, as it determines the signaling strength between neurons. Long-term potentiation and depression (LTP/LTD) processes modify the synaptic plasticity via neurotransmission.[1–4] In both cases, action potentials and redistributions of Ca^{2+} ions trigger the release of neurotransmitters from vesicles in the presynaptic membrane to the synaptic cleft. Receptors in the postsynaptic membrane capture and bind to the released neurotransmitters. Depending on the type of neurotransmitter, this either raises or lowers the postsynaptic potential and generates a postsynaptic current (PSC).

Emulation of the synaptic structure, neurotransmission process, and ensuing synaptic functions is essential for the realization of intelligent brain-like computing.[5–8] Inspired by the brain, several two-terminal ionic memristors have been proposed as artificial synapse.[9–30] One popular memristor-type relies on the formation and rupture of conductive filaments by field-driven and thermally assisted ion migration in insulating oxides (e.g., HfO_x, TiO_2, and SiO_2) sandwiched between two metals.[9–20] The dynamics of ion migration around conductive filaments in an insulating material, however, significantly differs from the synaptic neurotransmission process, whereby the release and bonding of neurotransmitters by two different entities (the pre- and postsynaptic membranes) modify the membrane potential.[31] Recently, physical realizations that emulate the dynamics or electrochemistry of biological processes more closely have been investigated to further advance the implementation of neuromorphic computing hardware. For example, the dynamics of Ca^{2+} in pre- and postsynaptic compartments has been successfully reproduced by second-order drift memristors based on oxide bilayers[32–34] and Ag nanocrystals,[35] and artificial neurons with stochastic leaky integrate-and-fire dynamics have been realized using Ag nanoparticles in a dielectric film.[36] Moreover, the quantal, stochastic, and excitatory or inhibitory nature of neurotransmitter release has been mimicked in a MoS_2 field-effect transistor.[37] Research activities on artificial synapses and neurons with biorealistic transport dynamics are motivated by a substantial reduction in footprint, complexity, and energy consumption, and an improved emulation of brain functions.

Here, we report on an alternative implementation of a biorealistic artificial synapse. Our approach is based on oxygen vacancy migration in tunnel junction memristors with a thin $SrTiO_3$

Dr. H. Tan, Dr. S. Majumdar, Dr. Q. Qin, Prof. S. van Dijken
Nanospin
Department of Applied Physics
Aalto University School of Science
P. O. Box 15100, FI-00076 Aalto, Finland
E-mail: hongwei.tan@aalto.fi; sebastiaan.van.dijken@aalto.fi

Dr. J. Lahtinen
Surface Science
Department of Applied Physics
Aalto University School of Science
P. O. Box 15100, FI-00076 Aalto, Finland

The ORCID identification number(s) for the author(s) of this article can be found under https://doi.org/10.1002/aisy.201900036.

DOI: 10.1002/aisy.201900036

(STO) tunnel barrier and one conducting $La_{0.67}Sr_{0.33}MnO_3$ (LSMO) electrode (**Figure 1**a). We show that reversible migration of oxygen vacancies across the STO/LSMO interface changes the barrier potential and, thereby, the tunneling current (Figure 1b), a process that mimics the release and bonding of neurotransmitters in a biological synapse and resulting changes of the PSC. In addition to the physical resemblance, the oxide tunnel junctions offer an excellent retention of intermediate resistance states and stable LTP/LTD, which are essential for memory and learning. We also demonstrate biorealistic quantal, stochastic, and excitatory or inhibitory characteristics of oxygen vacancy migration in our tunnel junction memristors by a systematic variation of the number, amplitude, and polarity of the voltage pulses. Other attractive features of ionically controlled tunnel junctions include self-limitation of oxygen vacancy migration to the tunnel barrier and a thin interface layer in the conducting oxide electrode (electric-field screening effect), access to a large number of distinct conductance states (large switching effect because of an exponential dependence on the tunnel barrier width and height), and high energy efficiency (operation using small tunneling currents). We also note that the ion migration process in our tunnel junctions deviates from other metal–insulator–metal (M–I–M) memristors that have been previously studied.[9–20] In most M–I–M realizations, the insulating layer is relatively thick, and ion migration is driven by combined effects of temperature and field gradients.[38] In our tunnel junction memristor, the insulating layer is 4 nm thin, and, consequently, the application of a few volts already produces an electric field of the order $10^6\,V\,cm^{-1}$. In this high-field regime, the ion drift velocity depends exponentially on the electric field.[39] We demonstrate that the field-controlled migration of oxygen vacancies in our tunnel junction memristor at low temperatures combines excellent stability of written resistance states and biorealistic emulation of key synaptic functions.

2. Results and Discussion

2.1. Tunnel Junction Memristor

The tunnel junction memristor consists of a 20 nm LSMO bottom electrode, a 4 nm STO tunnel barrier, and a 50 nm Au top electrode. The LSMO and STO layers were epitaxially grown on (001)-oriented STO substrates using pulsed laser deposition (PLD). After oxide film growth, the bilayers were patterned into solid tunnel junctions using photo- and e-beam lithography steps. During one of these steps, the Au top electrodes were defined by e-beam evaporation and liftoff. In the final structure (Figure 1a), the top and bottom electrodes were separated by 110 nm of insulating Ta_2O_5 to avoid shortening, and the junction area was $1 \times 2\,\mu m^2$. We performed all transport measurements at 5 K to ensure field-controlled migration of oxygen vacancies.

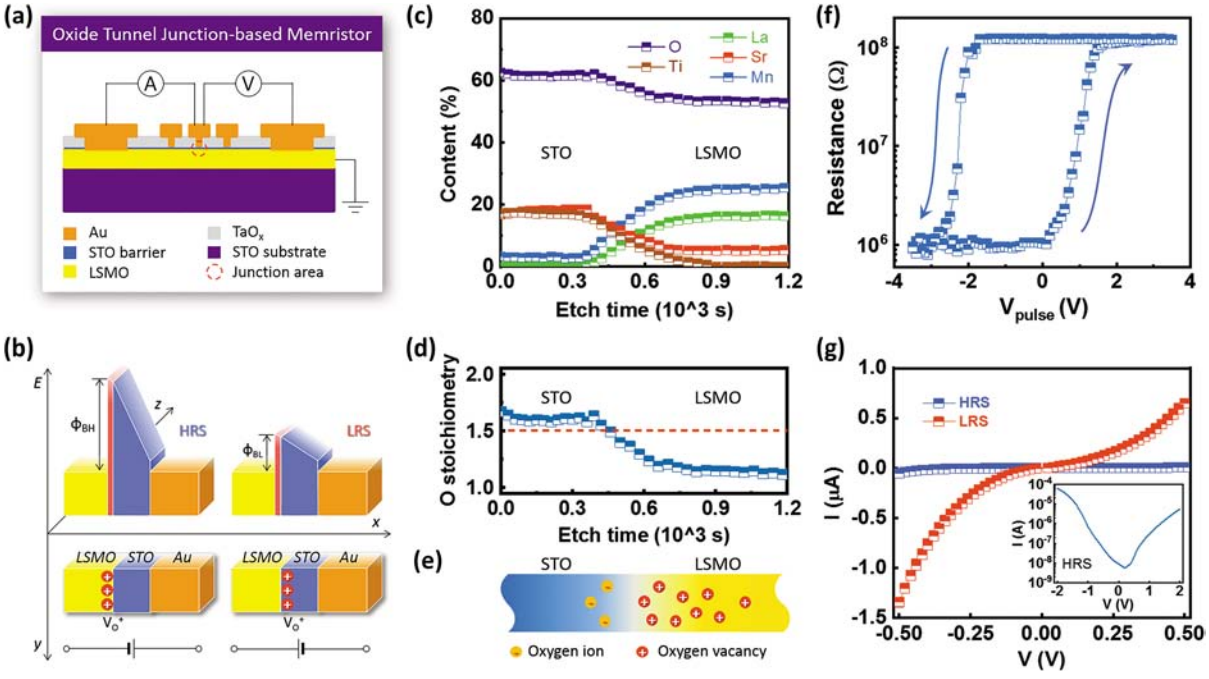

Figure 1. Structure, operation principle, and resistance switching of a tunnel junction memristor with an ionically active interface. a) Schematic of a patterned Au/STO/LSMO tunnel junction. The junction area is $1 \times 2\,\mu m^2$. In transport measurements, voltage pulses are applied to the Au top electrode, and the bottom LSMO layer is grounded. b) Schematic of the resistance switching mechanism. Switching is based on oxygen vacancy migration across the STO/LSMO interface. When oxygen vacancies are located in the interface layer of the LSMO electrode, the junction exhibits a HRS. Migration of the positively charged vacancies into the STO layer reduces the width and height of the tunnel barrier. As a result, the tunnel junction memristor switches to an LRS. c) XPS depth profile measurement of the atomic concentrations in a STO/LSMO bilayer. d) Effective oxygen stoichiometry, defined as the anion/cation concentration ratio, in the same bilayer. e) Schematic illustration of the as-grown STO/LSMO bilayer oxidation state. f) Resistance switching curve of a tunnel junction memristor measured using 30 ms triangular voltage pulses of varying amplitude. After each pulse, the junction resistance is read at a bias voltage of −0.1 V. g) Current–voltage curves for the HRS and LRS states.

More details on sample fabrication and characterization are given in the Experimental Section.

We specifically selected LSMO and STO as an electrode and a barrier material, respectively, because their electronic transport properties are inversely affected by oxygen vacancies. In optimally doped LSMO (La, 67%; Sr, 33%), metallic transport originates from hopping of e_g electrons between adjacent Mn^{3+} and Mn^{4+} ions. An increase in the oxygen vacancy concentration changes the Mn^{3+}/Mn^{4+} ratio and, thereby, the electrical resistance. Starting from optimally doped LSMO with the lowest resistance state, the introduction of oxygen vacancies shifts the effective doping level into the under-doped region of the LSMO phase diagram, in which metallic transport is gradually converted to more insulating behavior.[40,41] In our tunnel junction memristor, this effect increases the effective barrier width. In STO, oxygen vacancies change the Ti cation valency, leading to n-type doping and reduced electrical resistivity.[42] Moreover, angle-resolved photoemission spectroscopy (ARPES) experiments[43] and density functional theory (DFT) calculations[44] indicate that oxygen vacancy impurity levels in STO are located 0.8 eV below the bottom of the conduction band. These impurity levels reduce the effective height of the STO tunnel barrier. Since oxygen vacancies have an opposite effect on the electronic properties of LSMO and STO, the migration of oxygen vacancies across the STO/LSMO interface changes the barrier width and height of the tunnel junction memristor.[45] For instance, the migration of oxygen vacancies from the STO tunnel barrier into the LSMO electrode enhances the tunnel barrier width and height, causing an exponential increase in the junction resistance. Reversal of the migration direction has the inverse effect (Figure 1b).

To assess the oxygen stoichiometry of the as-grown STO/LSMO bilayer, we performed X-ray photoelectron spectroscopy (XPS) depth-profiling experiments. From the measurements, the atomic concentrations of the different cations and oxygen anions were calculated. Figure 1c shows depth-resolved information as a function of etch time for a 4 nm STO/20 nm LSMO bilayer. Details on the relative sensitivity factors used in the calculations of elemental concentrations are given in the Supporting Information. For stoichiometric growth, the oxygen concentration should be 60% in both oxides. In the as-grown bilayer, the oxygen concentration almost matches this nominal value in STO, whereas a substantial oxygen deficiency is measured in LSMO. In Figure 1d, the oxygen off-stoichiometry is plotted as the anion/cation ratio, which would correspond to 1.5 for a stoichiometric bilayer. The near nominal concentration of oxygen in STO and subnominal concentration of oxygen in LSMO most likely originates from the growth sequence. For single LSMO films, we do attain good stoichiometry using the same PLD parameters in combination with slow cooling in oxygen.[41] During the bilayer growth, the STO film is grown directly onto LSMO, and the sample is then cooled in oxygen. This process ensures near stoichiometry in the top STO layer but introduces an oxygen deficiency in LSMO. Figure 1e shows the oxidation state of the as-grown STO/LSMO bilayer. In this work, we reversibly move the reservoir of positively charged oxygen vacancies across the STO/LSMO interface by the application of voltage pulses, mimicking the role of neurotransmitters in a biological synapse and triggering ensuing changes in the postsynaptic-like tunneling current.

As a first step, we demonstrate bipolar resistance switching in our tunnel junction memristor (Figure 1f). In these measurements, we apply voltage pulses with a duration of 30 ms and sweep the pulse amplitude from −3.5 to +3.5 V and back. After each pulse, the junction resistance is read at −0.1 V. If a large enough positive pulse is applied to the Au top electrode, oxygen vacancies migrate from the STO barrier into the LSMO bottom electrode. This field-driven process increases the barrier width and height, and, consequently, raises the resistance of the tunnel junction memristor. Reversal of the voltage pulse polarity directs the oxygen vacancies back into the STO tunnel barrier, which re-establishes the low resistance state (LRS). The nonuniformity of the electric field across the tunnel junction memristor most likely explains the asymmetry of the resistance switching curve. At a given bias voltage, the electric field is largest across the STO barrier, and it decays quickly within the LSMO electrode. Since the oxygen vacancies are driven by the electric field, it is anticipated that they migrate from the STO barrier into the LSMO electrode at a smaller bias voltage than in the opposite direction. Because of this, the switching voltage is smaller for positive pulses. The decay of the electric field in the LSMO electrode also works as a self-limiting mechanism for vacancy migration. As a result, oxygen vacancies are confined to a thin LSMO interface layer in the high resistance state (HRS). The HRS/LRS ratio is ≈100. The resistance switching effect is reproducible over many cycles and between samples, and it decays with temperature because of thermally activated inelastic tunneling through defect states in the tunnel barrier (Figure S1 and S2, Supporting Information). Operation of the tunnel junction memristor above room temperature may require the use of a second non-ionically active barrier.

Figure 1g shows current–voltage curves for the HRS and LRS of the tunnel junction memristor. Because the barrier consists of a double layer (STO tunnel barrier plus a thin insulating LSMO interface layer), numerical methods are required to fit the transport curves. In previous studies,[45,46] we used the Tsu-Esaki (TE) method and showed that the nonlinear current–voltage curves of tunnel junctions with ionically active interfaces are characterized by direct tunneling through a double barrier at a small bias voltage. At a larger bias voltage where transport is dominated by Fowler–Nordheim tunneling, the current–voltage curve for the HRS is asymmetric (inset of Figure 1g). This asymmetry is only reproduced by numerical TE simulations if a much larger barrier height at the bottom STO/LSMO interface is assumed,[45,46] as schematically shown in Figure 1b.

2.2. Octal Memory

The emulation of memory and learning in an integrated neural network requires access to a large range of discrete conductance levels with a long-term stability. To explore the stability of multilevel resistance switching in our tunnel junction memristor, we varied the strength of the maximum positive voltage pulse from +1.0 to +1.6 V. The results in **Figure 2**a indicate that seven different nonvolatile states are accessed by this reset process. A large negative voltage pulse sets the tunnel junction memristor back to the LRS. Switching back and forth between all eight resistance states is reproducible (Figure 2b), and, once written, the

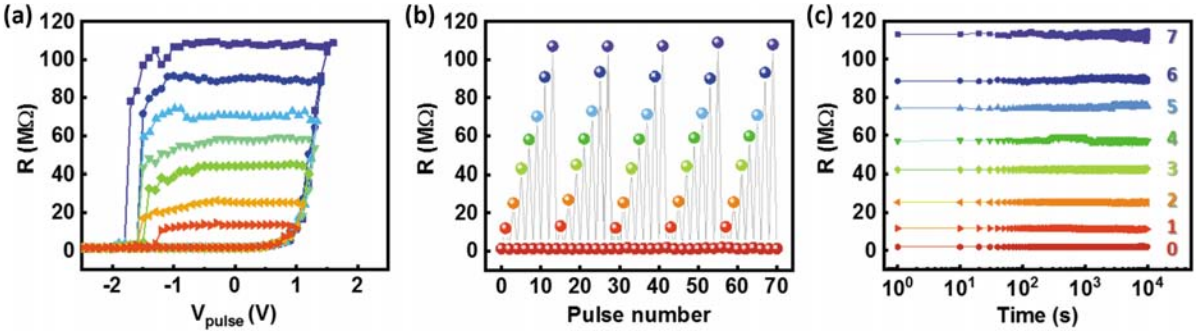

Figure 2. Multilevel resistance switching and retention. a) Writing of eight resistance states using reset voltage pulses ranging from +1.0 to +1.6 V. b) Reproducibility of multilevel resistance switching. After each reset pulse, the resistance is set back to the LRS using $V_{pulse} = -2.5$ V. c) Retention of the eight resistance states.

resistance levels remain stable for 10^4 s (Figure 2c). From an extrapolation of the measurement results in Figure 2c, we estimate a data retention time of at least 10 years. The strong retention of intermediate resistance states reinforces that oxygen vacancies are purely driven by a field-emission-like process at low temperatures. If the voltage pulse only suffices to migrate a fraction of the oxygen vacancies across the STO/LSMO interface, the newly established vacancy distribution is stable after the driving field is turned off. Figure S3, Supporting Information, shows current–voltage curves for the eight resistance states, and Figure S4, Supporting Information, demonstrates that eight discrete resistance levels can also be set by negative voltage pulses with amplitudes ranging from −1.7 to −2.4 V.

Next, we use the strong retention of resistance states in our tunnel junction memristor to proof the concept of an octal memory. In **Figure 3**a,b, we show that eight resistance states are written by voltage pulses V_0 to V_7 and that the junction resistance increases linearly with the reset pulse strength. This behavior provides fully deterministic programming capabilities. Using all eight levels, we construct an octal memory element. Compared with a conventional binary memory wherein a letter is coded by eight digits according to binary ASCII, an octal memory stores a letter using only three digits according to octal ASCII. For example, the letter "A" is stored as "0100 0001" in a binary memory, but as "101" in an octal memory. The lower number of required digits in an octal memory can be used to enlarge the storage density and capacity. Other letters of the alphabet are also represented by three digits in octal ASCII. By assigning octal values to regular intervals around the eight resistance levels, we demonstrate the writing and reading of the name "Aalto" in Figure 3c.

2.3. Synaptic Long-Term Plasticity

Having established the long-term stability of programmable resistance states, we now discuss the emulation of synaptic functions. In a biological synapse, neurotransmitters are released by action potentials and Ca^{2+} ion migration from vesicles at the presynaptic cell membrane. After their release, the neurotransmitters diffuse across the synaptic cleft and bind to receptors on the postsynaptic cell membrane (**Figure 4**a). Following other molecular processes, this ultimately changes the membrane potential and generates a PSC. Depending on the type of ionotropic neurotransmitter, for example, glutamate or gamma-aminobutyric acid (GABA), the PSC is either excited or inhibited. Oxygen vacancy transport across the STO/LSMO interface of our tunnel junction memristor physically resembles this process, with the oxygen vacancies acting as the neurotransmitters that are released by voltage pulses from either the STO or LSMO interface layer and captured by the other. Induced changes of the barrier potential mimic variations of the membrane potential, and the resulting tunneling current acts as the PSC. In the tunnel junction memristor, an excitatory response, that is, an increase in the tunneling current, is generated if oxygen vacancies migrate from LSMO to STO under negative voltage pulses. The tunneling current is inhibited when the migration direction is reversed by a positive voltage pulse (Figure 1b). Subsequent exhibitory and inhibitory behaviors by negative and positive voltage pulses are demonstrated in Figure 4b. Since all current levels are stable, these processes correspond to LTP/LTD, which are essential for long-term memory and learning.

The process of neurotransmitter release in the brain has three important characteristics, it is quantal, stochastic, and can be excitatory or inhibitory. Previously, Arnold et al. demonstrated that all these features are reproduced by the electronic transport in a back-gated MoS_2 field-effect transistor.[37] We assess the release properties of oxygen vacancies in our tunnel junction memristor using the same criteria. The quantal nature of neurotransmitter release is captured if the resulting PSC varies with the number of action potentials (N_{AP}). **Figure 5**a,b shows a strong dependence of the memristor tunneling current on the pulse number for voltages ranging from −2.2 to −2.4 V (exhibitory behavior) and +0.6 to +1.2 V (inhibitory behavior). Saturation of the signal mimics the situation where all vesicles at the presynaptic membrane release their neurotransmitters.

The stochastic nature of neurotransmitter release is caused by a finite chance of vesicle exocytosis. Because exocytosis is more likely for strong action potentials, the probability of neurotransmitter release should correlate with the pulse amplitude. In Arnold et al., the dynamic process of neurotransmitter release is described by PSC $\propto p_r n_T f(N_{AP})$, where p_r is the release probability, n_T is the number of neurotransmitters in each vesicle, and $f(N_{AP})$ is the number of vesicles released in response to N_{AP}.[37] Here, we use the measured postsynaptic-like tunneling

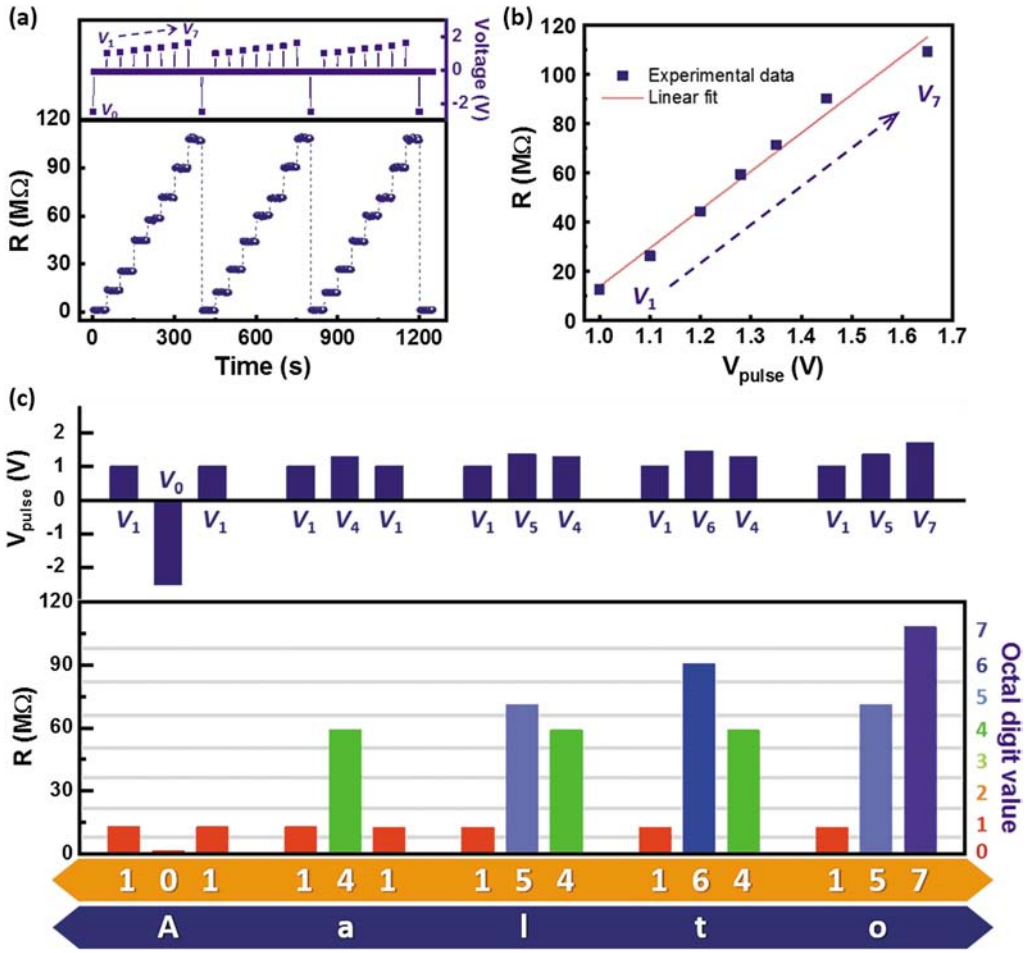

Figure 3. The tunnel junction memristor as an octal memory element. a) Programming of eight resistance levels by a sequence of voltage pulses. b) Demonstration of a linear variation of the junction resistance with the reset pulse amplitude. c) Proof-of-concept of a tunnel junction memory element storing the word "Aalto" in octal ASCII.

current to demonstrate the variation of PSC and p_r with voltage. Figure 5c,d shows the voltage dependence of the tunneling current in a memristor junction for 1, 5, and 10 pulses. From these data, we calculate a release probability (p_r) using $p_r = I_m/I_s$, where I_m and I_s are the measured and saturated tunneling current (Figure 5e,f). The curves indicate a swift change of the release probability with pulse amplitude, especially for negative voltages. The strong variation of the tunneling current (release probability) in our ionic tunnel junction memristor has several origins. First, the drift velocity of oxygen vacancies depends exponentially on the amplitude of the applied electric field.[39] Second, the ensuing changes in the width and height of the barrier potential affect the tunneling current in an exponential manner.[45,46] Based on these notions, an abrupt double-exponential-like increase or decrease in the tunneling current is anticipated in a narrow voltage range below saturation. Modeling of this relationship is complicated because of unknown factors such as the complex-dynamic many-body process of oxygen vacancy transport and unknown specifics about the variation of the tunnel barrier profile on a redistribution of oxygen vacancies at the STO/LSMO interface.

In biology, spike-timing-dependent plasticity (STDP) is a form of Hebbian learning induced by temporal correlations between the spikes of pre- and postsynaptic neurons.[47–49] Several types of STDP have been demonstrated in biological synapses.[49–52] The most common is asymmetric STDP, including Hebbian and anti-Hebbian learning rules.[50] Another is symmetric STDP, which has been shown to play a key role in reliable storage and the recall of information in the hippocampal CA3 network.[51] To emulate STDP in our tunnel junction memristor, we applied pre- and postspikes in the form of voltage pulses with a duration of 10 ms to the Au top electrode and LSMO bottom electrode, respectively. The results are summarized in **Figure 6**. The synaptic weight (Δw) of the junction, that is, the change in tunnel junction conductance, alters when the voltage maximum of the paired pulses exceeds the depression or potentiation threshold (Figure S5, Supporting Information). For the asymmetric pulses shown in Figure 6a, the weight of the junction is depressed if $\Delta t < 0$ and potentiated if $\Delta t > 0$. This behavior corresponds to the Hebbian learning rule. The synaptic response changes to anti-Hebbian learning if the asymmetric waveforms of the pre- and postspikes are reversed (Figure 6b). Symmetric STDP

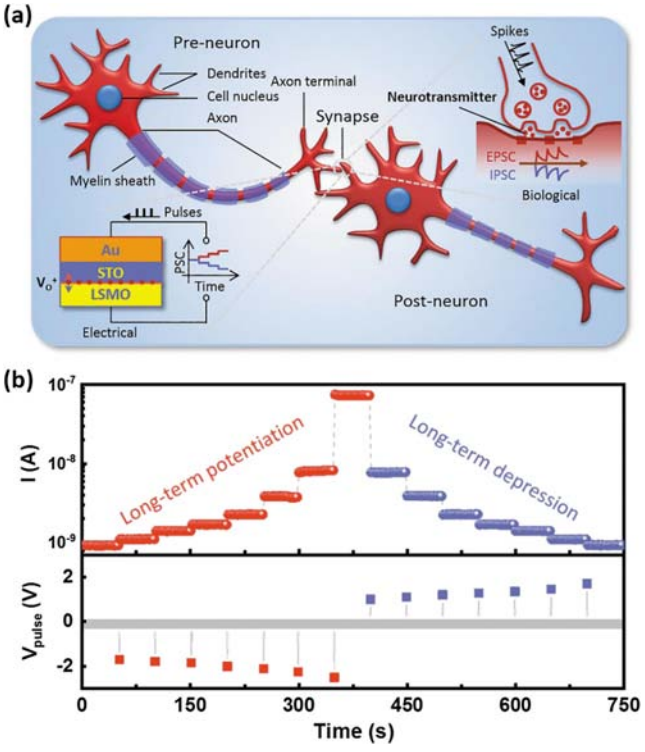

Figure 4. Emulation of synaptic LTP/LTD. a) Schematic of the tunnel junction memristor as a biorealistic emulator of neurotransmitter transport in a biological synapse. b) LTP and LTD for negative and positive voltage pulses, respectively. The duration of the voltages pulses is 30 ms.

where the synaptic weight is either increased or decreased by the application of two symmetric voltage pulses is also emulated by the tunnel junction memristor (Figure 6c,d). Oxygen vacancy migration in oxide tunnel junctions could therefore be used to accurately mimic different learning behaviors. We note that the pre- and postspikes in our experiments overlap, which is different from the brain.

Finally, we discuss the energy consumption of our tunnel junction memristor. The data presented in this article are obtained using voltage pulses with a duration of 10 or 30 ms. LTP/LTD and STDP behaviors require pulse amplitudes ranging from 1 to 2.5 V (Figure 4–6). The tunneling current at 1 V is about 5×10^{-7} A (inset of Figure 1g). Based on these parameters, the minimum energy consumption per operation is 5 nJ, which is several orders of magnitude larger than in the brain.[53] A reduction of the pulse duration would improve the energy efficiency of the tunnel junction memristor. In our previous work on LSMO-based tunnel junctions with a similar ionic interface,[45] we demonstrated that 100 ns voltage pulses still produce a large resistance switching effect.

3. Conclusions

Inspired by the release, diffusion, and bonding dynamics of neurotransmitters in biological synapses, we propose reversible electric-field-driven vacancy migration in an oxide tunnel junction memristor as a biorealistic emulator of these processes. In the tunnel junction memristor, oxygen vacancy transport across the LSMO/STO interface changes the barrier potential,

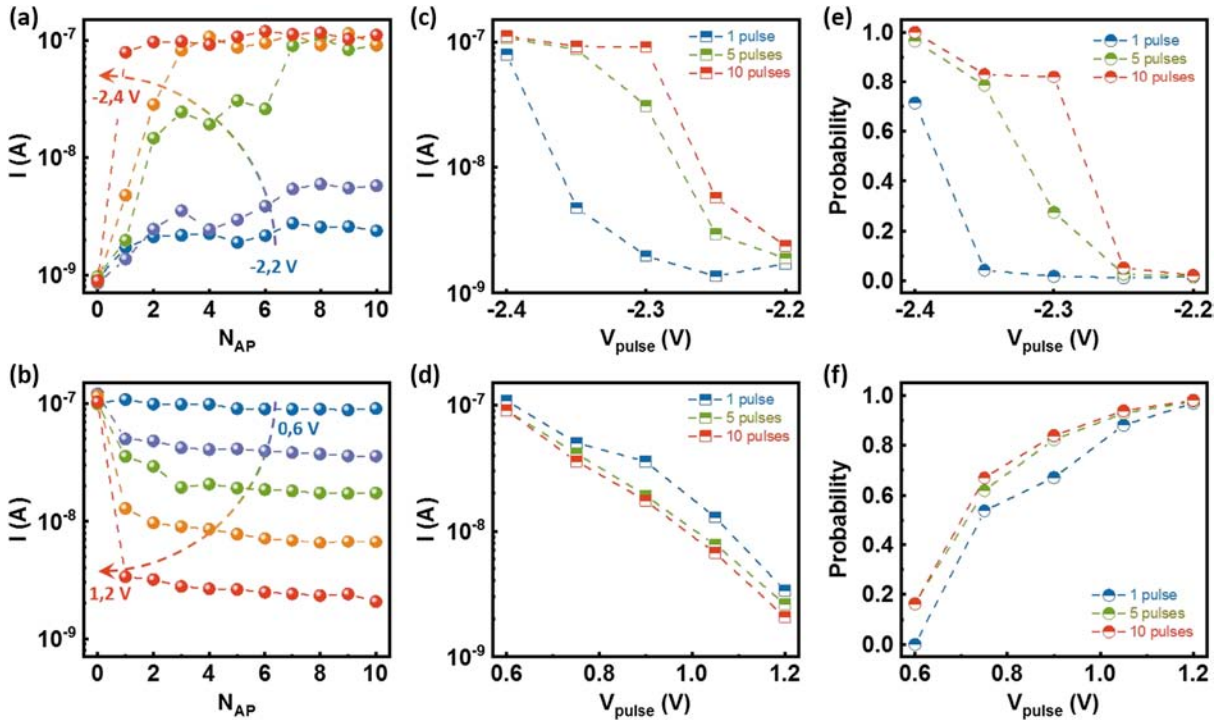

Figure 5. Modulation of long-term plasticity. a) Excitatory and b) inhibitory tunneling current as a function of the number of voltage pulses (i.e., the number of action potentials N_{AP}). c,d) Dependence of the tunneling current on pulse amplitude for excitatory and inhibitory responses. Data for trains of 1 pulse, 5 pulses, and 10 pulses are shown. e,f) Release probability as a function of pulse amplitude.

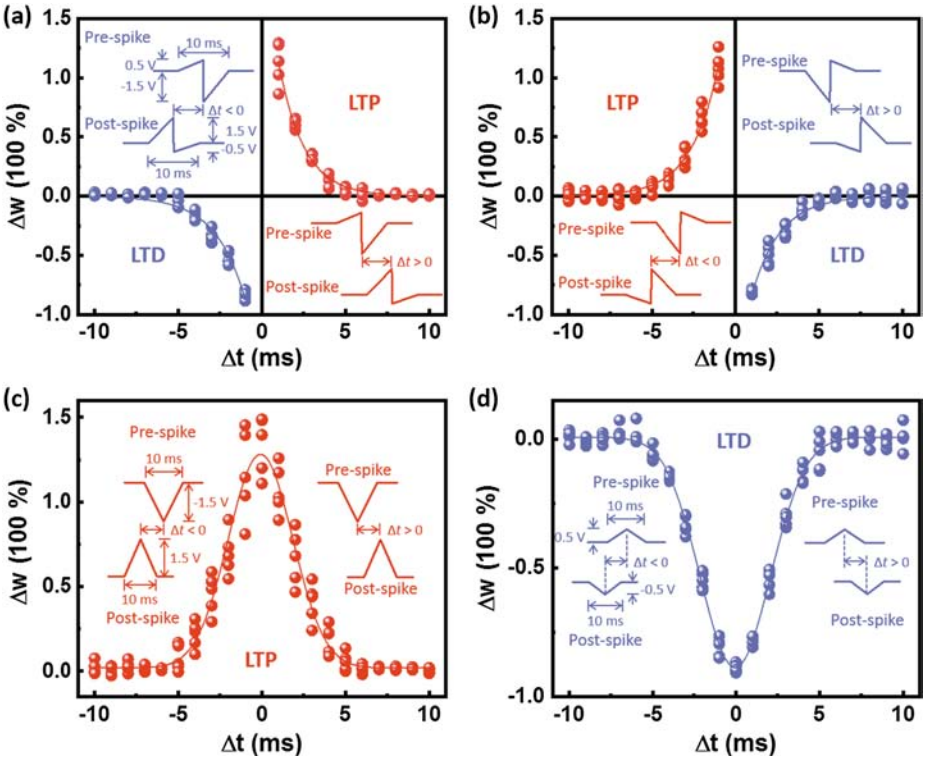

Figure 6. STDP. Asymmetric STDP of a) the Hebbian learning rule and b) the anti-Hebbian learning rule. The change of the synapse weight (Δw) is plotted as a function of the time difference (Δt) between the pre- and postspikes that are applied to the top and bottom electrode, respectively. The solid lines are exponential fitting curves to the experimental data. c,d) Symmetric STDP demonstrating LTP/LTD . The solid lines in these graphs are Gaussian fitting curves. The shape of the voltage spikes used in the STDP measurements is depicted as insets. In all measurements, a set pulse of −2.2 V is used to set the junction memristor to an intermediate resistance state.

and, thereby, the tunneling current. This activity closely mimics neurotransmitter transport from the pre- to the postsynaptic membrane, the change of the membrane potential, and the generation of a PSC. If operated under field-dominated migration conditions, the induced variations of the tunnel junction resistance are fully reproducible, nonvolatile, and durable, as demonstrated by proof-of-concept experiments on an octal memory and excellent LTP/LTD characteristics. The tunnel junction memristor also emulates the quantal, stochastic, and excitatory or inhibitory nature of neurotransmitter release and reproduces various learning rules in the STDP measurements. With all these attributes, the tunnel junction memristor proposed here offers a new physical approach to the design of intelligent memory, logic, and cognitive devices for brain-like computation.

4. Experimental Section

Device Fabrication and Material Characterization: Commercial (001)-oriented STO substrates were etched in buffered hydrogen fluoride (HF) for 30 s and annealed in oxygen atmosphere at 950 °C for 60 min to obtain TiO_2-terminated surfaces. The 20 nm-thick LSMO film acting as the bottom electrode was epitaxially grown on STO by PLD at 700 °C in an oxygen partial pressure of 0.5 mbar. Hereafter, the 4 nm-thick STO tunnel barrier was grown immediately on LSMO by PLD at the same temperature, but in a reduced oxygen partial pressure of 0.15 mbar. As the top electrode, a 50 nm-thick Au layer was deposited by e-beam evaporation. The trilayer was patterned into a large number of $1 \times 2\ \mu m^2$ tunnel junctions using a combination of photo- and e-beam lithography. During patterning, a 110 nm-thick Ta_2O_5 layer was used to electrically isolate the top and bottom electrodes. The contact pads of the tunnel junctions consisted of 500 nm Al/10 nm Au. A schematic of a patterned tunnel junction is shown in Figure 1a.

The XPS measurements were carried out using a Kratos Axis Ultra system. For depth profiling, a $2 \times 2\ mm^2$ area of the surface was sputtered with 5 keV Ar^+ ions in 40 s intervals corresponding to roughly 1 nm material removal. The measurements were performed with monochromatic Al Kα radiation (1486.7 eV). The analysis area had a diameter of 200 µm. Individual spectra of La 3d, Mn 2p, Ti 2p, Sr 3p, C1s, and O 1s were recorded with 80 eV pass energy and 100 meV energy step after every sputtering cycle. Shirley background correction was used.

Electrical Transport Measurements: Resistance switching effects and synaptic functions of the tunnel junction memristors were characterized at 5 K in a Janis SHI-4-1 cryostat system using a four-point measurement geometry. The resistance states of the junctions were read at −0.1 V using a sourceMeter (Keithley 2400) after the application of short voltage pulses (V_{pulse}) from an arbitrary function generator (Tektronix AFG 1062). For STDP measurements, voltage pulses of various shapes were preloaded onto the function generator. In all measurements except STDP, the LSMO bottom electrode was grounded, and the voltage pulses were applied to the Au top electrode. We used a current compliance of 0.1 mA to protect the junctions.

Supporting Information

Supporting Information is available from the Wiley Online Library or from the author.

Acknowledgements

The authors acknowledge the Academy of Finland (Grant Nos. 316857, 316973, and 13293916). The project made use of the Micronova Nanofabrication Center and the Aalto University Nanomicroscopy Center (Aalto-NMC), supported by Aalto University.

Conflict of Interest

The authors declare no conflict of interest.

Keywords

artificial synapses, ionic interface, long-term plasticity, memristors, neurotransmitter release, octal memory, oxide tunnel junction

Received: April 3, 2019
Revised: May 13, 2019
Published online: June 26, 2019

[1] T. V. P. Bliss, G. L. Collingridge, *Nature* **1993**, *361*, 31.
[2] H. Markram, J. Lübke, M. Frotscher, B. Sakmann, *Science* **1997**, *275*, 213.
[3] K. C. Martin, A. Casadio, H. Zhu, Y. E., J. C. Rose, M. Chen, C. H. Bailey, E. R. Kandel, *Cell* **1997**, *91*, 927.
[4] H. D. I. Abarbanel, R. Huerta, M. I. Rabinovich, *Proc. Natl. Acad. Sci. USA* **2002**, *99*, 10132.
[5] C. Mead, *Proc. IEEE* **1990**, *78*, 1629.
[6] C. Diorio, P. Hasler, B. A. Minch, C. Mead, *IEEE Trans. Electron Devices* **1996**, *43*, 1792.
[7] D. Kuzum, S. Yu, H.-S. P. Wong, *Nanotechnology* **2013**, *24*, 382001.
[8] P. A. Merolla, J. V. Arthur, R. Alvarez-Icaza, A. S. Cassidy, J. Sawada, F. Akopyan, B. L. Jackson, N. Imam, C. Guo, Y. Nakamura, B. Brezzo, I. Vo, S. K. Esser, R. Appuswamy, B. Taba, A. Amir, M. D. Flickner, W. P. Risk, R. Manohar, D. S. Modha, *Science* **2014**, *345*, 668.
[9] T. Chang, S.-H. Jo, W. Lu, *ACS Nano* **2011**, *5*, 7669.
[10] Y. Aoki, C. Wiemann, V. Feyer, H.-S. Kim, C. M. Schneider, H. Ill-Yoo, M. Martin, *Nat. Commun.* **2014**, *5*, 3473.
[11] M. Prezioso, F. Merrikh-Bayat, B. D. Hoskins, G. C. Adam, K. K. Likharev, D. B. Strukov, *Nature* **2015**, *521*, 61.
[12] S. L. Barbera, D. Vuillaume, F. Alibart, *ACS Nano* **2015**, *9*, 941.
[13] I. Gupta, A. Serb, A. Khiat, R. Zeitler, S. Vassanelli, T. Prodromakis, *Nat. Commun.* **2016**, *7*, 12805.
[14] Z.-H. Tan, R. Yang, K. Terabe, X.-B. Yin, X.-D. Zhang, X. Guo, *Adv. Mater.* **2016**, *28*, 377.
[15] C. Wu, T. W. Kim, T. Guo, F. Li, D. U. Lee, J. J. Yang, *Adv. Mater.* **2017**, *29*, 1602890.
[16] M. Ignatov, M. Zieler, M. Hansen, H. Kohlstedt, *Sci. Adv.* **2017**, *3*, e1700849.
[17] C. Yoon, J. H. Lee, S. Lee, J. H. Jeon, J. T. Jang, D. H. Kim, Y. H. Kim, B. H. Park, *Nano Lett.* **2017**, *17*, 1949.
[18] R. Yang, H.-M. Huang, Q.-H. Hong, X.-B. Yin, Z.-H. Tan, T. Shi, Y.-X. Zhou, X.-S. Miao, X.-P. Wang, S.-B. Mi, C.-L. Jia, X. Guo, *Adv. Funct. Mater.* **2018**, *28*, 1704455.
[19] D. S. Jeong, C. S. Hwang, *Adv. Mater.* **2018**, *30*, 1704729.
[20] M. A. Zidan, J. P. Strachan, W. D. Lu, *Nat. Electron.* **2018**, *1*, 22.
[21] S. H. Jo, T. Chang, I. Ebong, B. B. Bhadviya, P. Mazumader, W. Lu, *Nano Lett.* **2010**, *10*, 1297.
[22] T. Ohno, T. Hasegawa, T. Tsuruoka, K. Terabe, J. K. Gimzewski, M. Aono, *Nat. Mater.* **2011**, *10*, 591.
[23] Y. Yang, B. Chen, W. D. Lu, *Adv. Mater.* **2015**, *27*, 7720.
[24] B. Li, Y. Liu, C. Wan, Z. Liu, M. Wang, D. Qi, J. Yu, P. Cai, M. Xiao, Y. Zeng, X. Chen, *Adv. Mater.* **2018**, 1706395.
[25] D. Kuzum, R. G. D. Jeyasingh, B. Lee, H.-S. P. Wong, *Nano Lett.* **2012**, *12*, 2179.
[26] T. Tuma, A. Pantazi, M. L. Gallo, A. Sebastian, E. Eleftheriou, *Nat. Nanotechnol.* **2016**, *11*, 693.
[27] L. Q. Zhu, C. J. Wan, L. Q. Guo, Y. Shi, Q. Wan, *Nat. Conmmun.* **2014**, *5*, 3158.
[28] S. Boyn, J. Grollier, G. Lecerf, B. Xu, N. Locatelli, S. Fusil, S. Girod, C. Carrétéro, K. Garcia, S. Xavier, J. Tomas, L. Bellaiche, M. Bibes, A. Barthélémy, S. Saïghi, V. Garcia, *Nat. Commun.* **2017**, *8*, 14736.
[29] S. Majumdar, H. Tan. Q. H. Qin, S. van Dijken, *Adv. Electron. Mater.* **2019**, *5*, 1800795.
[30] S. Choi, S. H. Tan, Z. Li, Y. Kim, C. Choi, P.-Y. Chen, H. Yeon, S. Yu, J. Kim, *Nat. Mater.* **2018**, *17*, 335.
[31] R. M. Eccles, A. Lundberg, *Nature* **1957**, *179*, 1305.
[32] S. Kim, C. Du, P. Sheridan, W. Ma, S. Choi, W. D. Lu, *Nano Lett.* **2015**, *15*, 2203.
[33] C. Du, W. Ma, T. Chang, P. Sheridan, W. D. Lu, *Adv. Funct. Mater.* **2015**, *25*, 4290.
[34] J. Yin, F. Zeng, Q. Wan, F. Li, Y. Sun, Y. Hu, J. Liu, G. Li, F. Pan, *Adv. Funct. Mater.* **2018**, *28*, 1706927.
[35] Z. Wang, S. Joshi, S. E. Savel'ev, H. Jiang, R. Midya, P. Lin, M. Hu, N. Ge, J. P. Strachan, Z. Li, Q. Wu, M. Barnell, G.-L. Li, H. L. Xin, R. S. Williams, Q. Xia, J. J. Yang, *Nat. Mater.* **2017**, *16*, 101.
[36] Z. Wang, S. Joshi, S. Savel'ev, W. Song, R. Midya, Y. Li, M. Rao, P. Yan, S. Asapu, Y. Zhuo, H. Jiang, P. Lin, C. Li, J. H. Yoon, N. K. Upadhyay, J. Zhang, M. Hu, J. P. Strachan, M. Barnell, Q. Wu, H. Wu, R. S. Williams, Q. Xia, J. J. Yang, *Nat. Electron.* **2018**, *1*, 137.
[37] A. J. Arnold, A. Razavieh, J. R. Nasr, D. S. Schulman, C. M. Eichfeld, S. Das, *ACS Nano* **2017**, *11*, 3110.
[38] J. J. Yang, D. B. Strukov, D. R. Stewart, *Nat. Nanotechnol.* **2013**, *8*, 13.
[39] D. B. Strukov, R. S. Williams, *Appl. Phys. A* **2009**, *94*, 515.
[40] P. Orgiani, A. Y. Petrov, R. Ciancio, A. Galdi, L. Maritato, B. A. Davidson, *Appl. Phys. Lett.* **2012**, *100*, 042404.
[41] L. Yao, S. Inkinen, S. van Dijken, *Nat. Commun.* **2017**, *8*, 14544.
[42] D. Kan, T. Terashima, R. Kanda, A. Masuno, K. Tanaka, S. Chu, H. Kan, A. Ishizumi, Y. Kanemitsu, Y. Shimakawa, M. Takano, *Nat. Mater.* **2005**, *4*, 816.
[43] W. Meevasana, P. D. C. King, R. H. He, S.-K. Mo, M. Hashimoto, A. Tamai, P. Songsiriritthigul, F. Baumberger, Z.-X. Shen, *Nat. Mater.* **2011**, *10*, 114.
[44] C. Lin, A. A. Demkov, *Phys. Rev. Lett.* **2013**, *111*, 217601.
[45] Q. H. Qin, L. Äkäslompolo, N. Tuomisto, L. Yao, S. Majumdar, J. Vijayakumar, A. Casiraghi, S. Inkinen, B. Chen, A. Zugarramurdi, M. Puska, S. van Dijken, *Adv. Mater.* **2016**, *28*, 6852.
[46] N Tuomisto, S. van Dijken, M. Puska, *J. Appl. Phys.* **2017**, *122*, 234301.
[47] R. E. Brown, P. M. Milner, *Nat. Rev. Neurosci.* **2003**, *4*, 1013.
[48] N. Caporale, Y. Dan, *Annu. Rev. Neurosci.* **2008**, *31*, 25.
[49] J. A. D'amour, R. C. Froemke, *Neuron* **2015**, *86*, 514.
[50] G. Koch, V. Ponzo, F. D. Lorenzo, C. Caltagirone, D. Veniero, *J. Neurosci.* **2013**, *33*, 9725.
[51] R. K. Mishra, S. Kim, S. J. Guzman, P. Jonas, *Nat. Commun.* **2016**, *7*, 11552.
[52] H. Norimoto, K. Makino, M. Gao, Y. Shikano, K. Okamoto, T. Ishikawa, T. Sasaki, H. Hioki, S. Fujisawa, Y. Ikegaya, *Science* **2018**, *359*, 1524.
[53] J. J. Harris, R. Jolivet, D. Attwell, *Neuron* **2012**, *75*, 762.